RSC Advances

ROYAL SOCIETY OF CHEMISTRY

www.rsc.org/advances

towards visible light.[22–27] Furthermore, the bismuth tungstate, Bi_2WO_6 which is formed by heating a mixture of Bi_2O_3 and WO_3 in a 1/1 molar ratio at temperatures higher than 900 °C was also reported to have good photocatalytic properties.[28,29] Taking this into account, a composite of WO_3 coated with Bi_2O_3 served as the basis for this study. Since WO_3 and Bi_2O_3 are both visible light driven photocatalysts, the Bi_2O_3/WO_3 composite was explored as a candidate for efficient photocatalytic activity under visible light.

In this work, a novel visible light active Bi_2O_3/WO_3 composite was synthesized using a hydrothermal process. The 1/1 molar ratio was chosen with the rational that upon heating at higher temperature, Bi_2WO_6 will be obtained and its photocatalytic properties can then be studied. The photocatalysts were characterized by PXRD, TGA/DSC, STEM, SEM-EDS, TEM, DRS, Raman, PL, EIS, and BET. Their photocatalytic performance was evaluated using the photocatalytic reduction of 4-nitroaniline (4-NA), and degradation of Rhodamine B (RhB) under visible light ($\lambda \geq 420$ nm). The heterostructured composite photocatalysts showed superior activity compared to pristine tungsten oxide, bismuth oxide, and ternary bismuth tungstate. A possible mechanism for the enhancement of photocatalytic activity of Bi_2O_3/WO_3 composite is proposed using band position calculations, electrochemical impedance, and photoluminescence data.

2. Experimental Section

2.1 Synthesis

2.1.1 Reagents

All chemicals used were analytical grade reagents and were used as received: Sodium tungstate ($Na_2WO_4{\cdot}2H_2O$, 99.7%, J.T. Baker Chemicals, USA), Bismuth nitrate ($Bi(NO_3)_3{\cdot}5H_2O$, 99%, Johnson Matthey Electronics, USA), Hexadecyl-trimethyl ammonium bromide (CTAB, 98%, Alfa Aesar, UK), Ethylene glycol ($C_2H_6O_2$, EG, >95%, Fisher Scientific, USA), Glycerol ($C_3H_8O_3$, 99.5%, Fisher Scientific, USA), hydrochloric acid (HCl, Fisher Scientific, USA), and pure ethanol (Pharmaco-AAPER, USA).

2.1.2 Synthesis of WO_3 nanoparticles

WO_3 nanoparticles were prepared according to a previously reported method with some modifications.[30] In a typical procedure, 1.0 g (3.03 mmol) of $Na_2WO_4{\cdot}2H_2O$ was dissolved in 10 mL of distilled water. 0.25 g (0.68 mmol) of CTAB was added to 5 mL of distilled water to make a clear solution. Subsequently, the two solutions were combined to obtain a clear solution. A yellow dispersion was formed after conc. HCl (3 mL) was added dropwise under constant magnetic stirring for 30 min. The yellow slurry was heated at 70 °C for 3 hours to obtain a yellow solid which was filtered, washed with deionized water and ethanol before drying under vacuum at 60 °C. The final dry mass was calcined at 400 °C for 4 hours to obtain pure WO_3 nanoparticles as confirmed by PXRD.

2.1.3 Preparation of Bi_2O_3/WO_3 composite and ternary oxide (Bi_2WO_6)

To obtain the composite, 2 mmol (0.97 g) of $Bi(NO_3)_3{\cdot}5H_2O$ was dissolved in a 60 ml mixture of water, glycerol and ethylene glycol (1:1:1) under constant magnetic stirring to obtain a clear solution. 1 mmol (0.23 g) of WO_3 nanoparticles were then added while stirring. The mixture was sonicated for 30 min, then transferred to a Teflon-lined stainless steel autoclave with an inner volume capacity of 100 mL. The autoclave was sealed and placed in an oven at 160 °C for 5 h to deposit Bi_2O_3 over WO_3. The solid obtained was separated by filtration and washed with distilled water and pure ethanol to remove any organics and dried under vacuum at 60 °C. A bright yellow Bi_2O_3/WO_3 composite was obtained after calcination at 400 °C for 2 hours (0.68 g, ~ 97 % yield based on the weight of bismuth nitrate and WO_3 used). Pure Bi_2O_3 was also prepared similarly without adding WO_3. A portion of the composite was calcined at 900 °C to obtain bismuth tungstate, Bi_2WO_6 as confirmed by PXRD.

To evaluate the role of heterojunction in the photocatalytic activity of Bi_2O_3/WO_3 composite photocatalysts, a mechanically mixed Bi_2O_3 and WO_3 sample (blend) with 1 to 1 molar ratio was also prepared.

2.2 Characterization

Bi_2O_3, WO_3, Bi_2O_3/WO_3 composite, and Bi_2WO_6, compounds were characterized by powder X-ray diffraction (PXRD) using a Bruker D8 diffractometer equipped with CuK_α radiation (λ = 1.5418 Å) in the range of $2\theta = 10–60°$. The morphologies and structures of the obtained samples were determined with an SEM using a Hitachi S-4800 FEG-SEM at 5 KV and a scanning transmission electron microscope (STEM, JEOL 2200-FS) with aberration corrected at 200 KV. The chemical composition of the samples was determined by an X-ray energy dispersion spectrometer (EDS, Bruker X-Flash, 30 mm^2 SDD) attached to the STEM. X-ray photoelectron spectroscopy (XPS) was performed using a Perkin Elmer PHI 570 ESCA/SAM System with an Al Kα source operating at 15 kV and 300 W power output to probe the elemental composition of the surface. Diffuse reflectance UV-vis spectra were collected on a Cary 5000 instrument equipped with a praying mantis kit in the range of 200 to 800 nm. Differential scanning calorimetry (DSC) and thermogravimetric analysis (TGA) were performed on a SDT-Q600 (TA instrument, USA) from 32-1000 °C under air flow and heating rate of 10 °C/min. Nitrogen adsorption–desorption isotherms at 77 K were investigated using an autosorb-iQ instrument from Quantachrome. Raman scattering was collected on a triple Raman spectrometer (Princeton Instruments Acton Trivista-555) customized with an ellipsoidal mirror and directed by a fiber optics bundle (Princeton Instruments) using a 532 nm laser source. Photoluminescence (PL) spectra were measured on the dual grating Fluorometer-3T (JY Horiba), with right angle configuration of excitation and detection. The excitation was made with 300 nm monochromatic light, with slits on the excitation and detection monochromators set at 5 nm.

Electrochemical Impedance Spectroscopy (EIS) measurements were conducted with a Gamry 3000 electrochemical workstation. The Spectra were collected using the conventional three-electrode system consisting of a modified indium-tin oxide (ITO) glass as the working electrode, Ag/AgCl as the reference electrode, and platinum wire as the counter electrodes. The EIS measurements were performed between 100kHz – 0.1 Hz at 0.25 V in a 0.1 M KCl solution with 5 mM $Fe(CN)_6^{3-}$/ $Fe(CN)_6^{4-}$ with an amplitude of 10 mV. The modified ITO working electrode was prepared by dispersing 7 mg of each photocatalyst sample in 1.0 mL of 18.2 Milli-Q water, dripping 80 µL of the slurry on ITO glass (dimensions: 1 cm × 1 cm), and drying the modified ITO working electrode in a vacuum oven at 60 °C for 5 hours prior to the measurement.

2.3 Photocatalytic test and Electrochemical Impedance spectroscopy (EIS)

The photocatalytic activity of the catalysts was evaluated by measuring the photocatalytic reduction of 4-nitroaniline (4-NA) and photocatalytic degradation rate of Rhodamine B (RhB) and under visible light irradiation. In a typical experiment, 80 mg of photocatalyst was dispersed in 50 mL of 4-NA aqueous solution (10 ppm) or RhB aqueous solution (10 ppm) in an 80 mL capacity quartz glass photo-reactor cell. The suspension was stirred in the dark for 30 min before turning on the lamp to establish an adsorption–desorption equilibrium. A 300 W Xenon lamp equipped with a UV cut-off filter ($\lambda \geq 420$ nm) was used as a source of visible light. The degradation of 4-NA was performed under nitrogen (flow rate of 50 mL/min) in the presence of 10 mg of ammonium oxalate. 1 mL of the suspension was withdrawn at predetermined time intervals (30 min. or 60 min.) and the catalyst was separated by centrifugation. The change in 4-NA and RhB concentrations were monitored using an Agilent-8453 UV-Vis spectrometer at λ = 380 nm (for 4-NA) and λ = 553 nm (for RhB). In order to detect the active species generated in the photocatalytic process, the scavengers, including disodium ethylene diamine tetra acetate (Na_2-EDTA), 1,4-benzoquinone (BQ) and isopropyl alcohol (IPA) were added as quenchers of holes (h+), superoxide radicals ($^{\bullet}O_2^-$), and hydroxyl radicals ($^{\bullet}OH$) respectively. All the experiments with scavengers were conducted in a similar manner of RhB degradation using Bi_2O_3/WO_3 composite photocatalyst (80 mg) using visible light as explained above. Fresh RhB solutions were replaced in each experiment. The effects of scavengers were concluded based on the percentage degradation of RhB by Bi_2O_3/WO_3 composite photocatalyst in 3 hours of visible light ($\lambda \geq 420$ nm) irradiation.

3. Results and discussion

3.1 Characterization of photocatalysts

The identity and purity of prepared WO_3, Bi_2O_3, Bi_2O_3/WO_3 composite, and Bi_2WO_6 were determined using PXRD as shown on Fig. 1. PXRD data indicate that the observed diffraction peaks of Bi_2O_3/WO_3 sample are in good agreement with those of monoclinic WO_3 (JCPDS-072-0677) and monoclinic Bi_2O_3 (JCPDS-070-8243). No additional peaks were observed, as confirmed by comparing Fig. 1a-c. The Bi_2O_3/WO_3 composite exhibits peaks from both Bi_2O_3 and WO_3 without any impurity peak. Fig. 1d corresponds to orthorhombic phase of Bi_2WO_6 (JCPDS-079-2381). The refined lattice parameters along with space groups of Bi_2O_3, WO_3 and Bi_2WO_6 are summarized in Table 1.

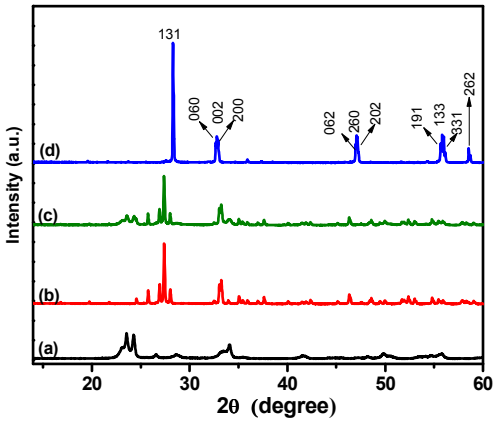

Fig.1: PXRD patterns of (a) WO_3, (b) Bi_2O_3, (c) Bi_2O_3/WO_3 composite and (d) Bi_2WO_6.

To further examine the Bi_2O_3/WO_3 composite, the morphology and microstructure were investigated by electron microscopy. SEM images of the Bi_2O_3/WO_3 composite are shown in Fig. 2a and b with different resolutions. SEM images revealed that the composite calcined at 400 $^{\circ}$C consists of elongated and spherical shapes particles, approximately 40-60 nm. Also, cauliflower like microstructures with 200-300 nm in size are evenly distributed in the sample. To further confirm the heterojunction composition, the samples were characterized by STEM analysis. The STEM study of pure samples (Fig. 3a and b) shows that the as prepared Bi_2O_3 has spherical morphology with particle size between 70 and 90 nm, while the as synthesized WO_3 is a mixture of spherical and needle shaped particles with size between 40 and 60 nm.

Table 1: Crystal structure representation, refined lattice parameters, band gaps and colour of Bi_2O_3, WO_3 and Bi_2WO_6.

Sample	Bi_2O_3	WO_3	Bi_2WO_6
Crystal system	monoclinic	monoclinic	orthorhombic
Crystal structure representation	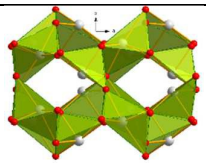	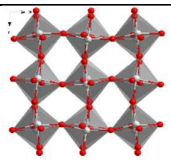	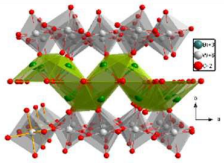
Space group	$P\,2_1/c$	$P\,2_1/n$	$P\,ca2_1$
Refined lattice parameters	a = 5.8481(2) Å b = 8.1651(2) Å c = 7.50921(3) Å β = 113.57(2) $^{\circ}$	a = 7.3124(4) Å b = 7.5294(3) Å c =7.6924(2) Å β = 90.658(3) $^{\circ}$	a = 5.4443(8) Å b = 16.4391(7) Å c = 5.4603(2) Å
Band gaps	2.80 eV	2.78 eV	2.93 eV
Color	yellow	yellow	white

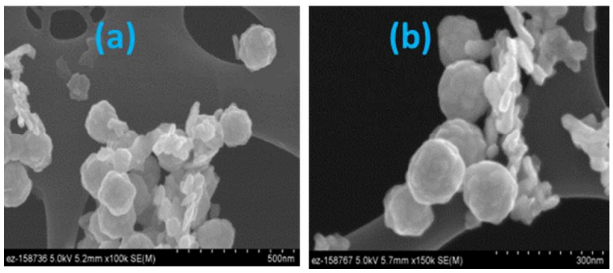

Fig. 2: (a) and (b) SEM images of Bi_2O_3/WO_3 composite.

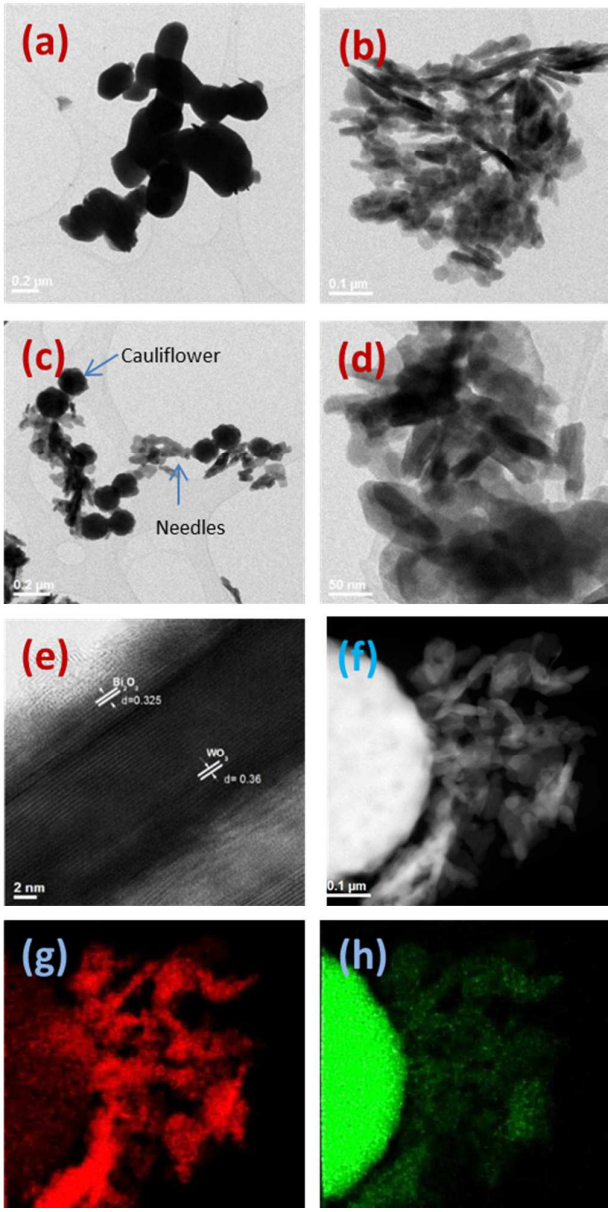

Fig. 3: STEM images of (a) Bi_2O_3, (b) WO_3, (c, d, e and f) Bi_2O_3/WO_3 composite, and (g, h) STEM mapping analysis for the composite shown in (f), Bi (green) and W (red).

STEM images of Bi_2O_3/WO_3 composite as shown in Fig. 3c-f show cauliflower-like structures (200-300 nm in size) as well as smaller particles (40-60 nm) evenly distributed throughout the composite. STEM-EDX mapping (Fig. 3f-h) on Bi_2O_3/WO_3 composite microcrystalline powders, show that tungsten and bismuth are evenly distributed throughout the composite. In addition to even distribution of the two oxides, elemental mapping clearly shows that the cauliflower-like structures contain more bismuth oxide, while the rod-like and spherical particles contain more tungsten oxide than bismuth oxide. The observed lattice fringes with inter-planar spacing of 0.325 and 0.361 nm calculated from high resolution STEM images (Fig. 3e), correspond to the (120) interplanar distance of the monoclinic phase of Bi_2O_3 and the (200) interplanar spacing of the monoclinic phase of WO_3 respectively. This result is consistent with that obtained from the PXRD analysis shown in Fig. 1.

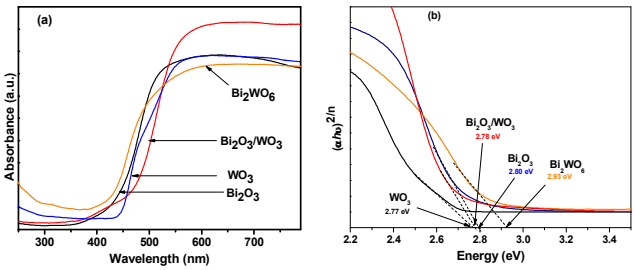

Fig. 4: (a) Diffuse reflectance spectra of composite, its components, and ternary oxide, Bi_2WO_6; (b) Plot of $(\alpha h\nu)^{2/n}$ vs energy ($h\nu$) for the determination of the band gap energy of WO_3, Bi_2O_3, and Bi_2WO_6. The extrapolation of the $(\alpha hv)^{2/n}$ vs. (hv) plot on the x intercepts gives optical band gaps.

Diffuse reflectance UV-Vis spectra of Bi_2O_3, WO_3, Bi_2O_3/WO_3 composite, and Bi_2WO_6 (Fig. 4) display photo-absorption properties at wavelength shorter than 443 nm, 447 nm, 446 nm and 423 nm, respectively. This clearly demonstrates that the composite and other studied catalysts had potential applications in the visible light region ($\lambda \geq 420$ nm). The band gap energy of a semiconductor may be calculated from Equation 1.[31]

$$ahv = A(hv - Eg)^{n/2} \quad (1)$$

Where α, h, v, Eg and A are the absorption coefficient, the Planck's constant, the light frequency, band gap energy, and a proportionality constant, respectively. The exponent n is determined by the type of optical transition of a semiconductor (n = 1 for direct transition and n = 4 for indirect transition). Thus, the band-gap energies (Eg) of the samples could be estimated from plots of $(ahv)^{2/n}$ versus the photon energy (hv). The value of n is taken as 1 for Bi_2O_3, and Bi_2WO_6 and 4 for WO_3.[32–36] In the case of Bi_2O_3/WO_3 composite, n=4 was used, assuming that the composite was an indirect band gap semiconductor. From the plot of $(ahv)^{2/n}$ versus (hv) (Fig. 4b), *the band gap* of Bi_2O_3, WO_3, Bi_2O_3/WO_3 composite, and Bi_2WO_6 were determined to be 2.80 eV, 2.77 eV, 2.78 eV, and 2.93 eV, respectively.

The DSC-TGA curves of Bi_2O_3/WO_3 composite (Fig. 5) show a major weight loss (approx. 10.5 %) before 400 ^{o}C, which can be attributed to dehydration and thermal decomposition of residual organic

molecules present in the precursors used during the synthesis of the Bi_2O_3/WO_3 composite. The DSC curve of the as prepared Bi_2O_3/WO_3 composite, shows three major endothermic peaks at 250 °C, 320 °C and 360 °C which may be assigned to loss of organics to form the Bi_2O_3/WO_3 composite. Another endothermic peak at 830 °C is attributed to the formation and crystallization of Bi_2WO_6. Based on the DSC-TGA data, the as prepared composite was calcined first at 400 °C to form the composite, and at 900 °C to obtain Bi_2WO_6. The identity of the phases obtained was confirmed by PXRD as shown on Fig. 1. The formation of pure ternary phase (Bi_2WO_6) from the composite further supports the 1 to 1 molar ratio of Bi_2O_3 and WO_3 in composite (Equation 2).

$$Bi_2O_3 + WO_3 \rightarrow Bi_2WO_6 \quad (2)$$

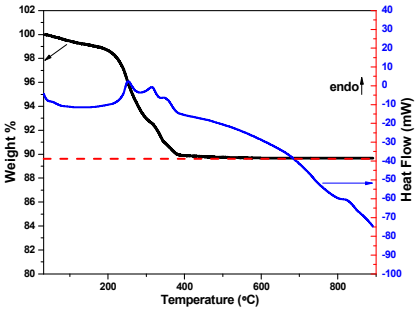

Fig. 5: TGA and DSC data of the Bi_2O_3/WO_3 composite.

XPS spectra of Bi_2O_3, WO_3, and Bi_2O_3/WO_3 composite (Fig. 6) indicate the presence of W, O, and Bi in the Bi_2O_3/WO_3 composite. The binding energy of the WO_3 sample was found to be about 38.7 eV, which corresponds to $4f_{7/2}$ of W(VI).[37,38] The two peaks observed at 160.09 and 165.80 eV correspond to the $4f_{7/2}$ and $4f_{5/2}$ of Bi(III), respectively, and are consistent with previously reported binding energies for Bi_2O_3.[39,40] The binding energies of bismuth and tungsten in the composite are slightly shifted when compared to those found for pure samples, which may be attributed to the intimate contact between the Bi_2O_3 and WO_3 particles.[41]

BET surface area measurements were collected for all samples using nitrogen adsorption–desorption isotherms as shown in Fig. 3S (†ESI). The results indicate that the specific surface area of composite (8.27 m^2/g) is slightly smaller than that of WO_3 (10.79 m^2/g), which may be due to particles agglomeration upon calcination. On the other hand, the surface area of composite is higher than that of pure Bi_2O_3 (6.46 m^2/g). The specific surface area of bismuth tungstate (0.74 m^2/g) is also small due to aggregation of Bi_2WO_6 particles upon calcination at 900 °C.

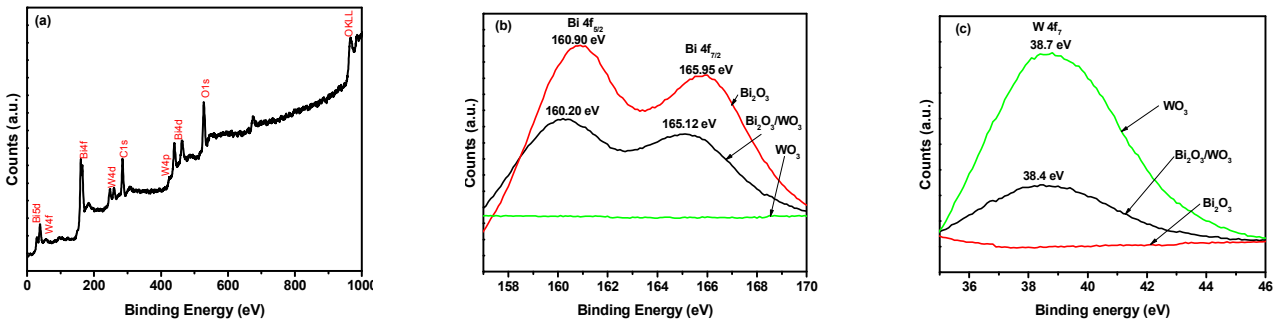

Fig. 6: (a) XPS survey spectra for Bi_2O_3/WO_3 composite. (b) XPS spectra of Bi 4f region for WO_3, Bi_2O_3, and Bi_2O_3/WO_3 composite. (c) XPS spectra of W 4f region for WO_3, Bi_2O_3, and Bi_2O_3/WO_3 composite.

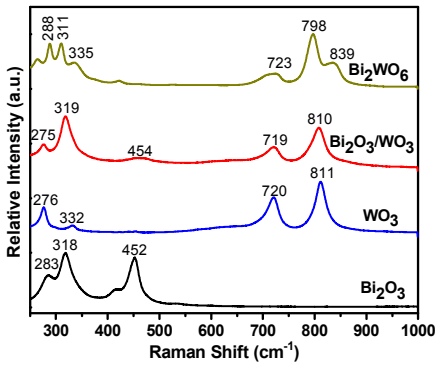

Fig. 7: Raman spectra of Bi_2O_3, WO_3, Bi_2O_3/WO_3 composite, and Bi_2WO_6.

Raman spectroscopy of WO_3, Bi_2O_3, Bi_2O_3/WO_3 composite and Bi_2WO_6 (Fig. 7) was performed to determine the changes of vibrational modes of Bi_2O_3 and WO_3 in the composite. The Raman data for pure WO_3 sample has absorption bands at 276 and 332 cm^{-1}, which are attributed to W-O-W bending vibrational modes; two other bands observed at 720 and 811 cm^{-1} are assigned to W-O-W stretching vibrations.[42] Similarly, the bands observed at 283, 319 and 452 cm^{-1} are due to the presence of Bi_2O_3.[43,44] The Bi_2O_3/WO_3 composite contains only bands of pure Bi_2O_3 and WO_3, which indicates that the composite consists of only these two oxides. Furthermore, the absorption becomes broader and weaker when WO_3 is covered with Bi_2O_3 in the composite which suggests increased crystalline defects within the framework. Such defects may favour the capture of photo-generated electrons and inhibit charge carriers recombination.[17] For Bi_2WO_6, the bands observed at 288, 311, 335, 723, 798, and 839 cm^{-1} correspond to the orthorhombic phase of Bi_2WO_6.[45,46]

3.2 Photocatalytic Testing

3.2.1 Activity

The photocatalytic activities of all synthesized compounds were evaluated under visible light illumination ($\lambda \geq 420$ nm) by comparing the photocatalytic reduction 4-NA, and degradation efficiencies of RhB (Fig. 8). Fig. 4S (supporting info) shows the photocatalytic degradation of RhB by the Bi_2O_3/WO_3 composite under visible light irradiation. A decrease of RhB absorption intensity at wavelength 553 nm is observed. Fig. 8a shows the photocatalytic degradation efficiency of RhB with different catalysts under visible light irradiation. In the absence of photocatalyst, photolysis of RhB is negligible. Pure Bi_2O_3 and pure WO_3 can degrade RhB by 38.07 % and 41.37% in 180 min, respectively, while the ternary oxide Bi_2WO_6 only degraded 27.15% of RhB when irradiated by visible light for the same period of time. In contrast 76.67% of RhB decomposed after 180 min visible light irradiation in the presence of Bi_2O_3/WO_3 composite. The Bi_2O_3/WO_3 composite exhibited significantly higher photocatalytic activity compared to pure Bi_2O_3, pure WO_3, and Bi_2WO_6. For 4-nitroanilne (4-NA), 60% of 4-NA decomposed after five hours irradiation by visible light in the presence of the Bi_2O_3/WO_3 composite, compared to only 18%, 25%, and 15% when equal amounts of Bi_2O_3, WO_3, and Bi_2WO_6 were used respectively (Fig. 8b). This result clearly indicates that the Bi_2O_3/WO_3 composite photocatalyst possesses superior photocatalytic capability in comparison to individual components as well as the ternary oxide. It is notable that blend sample (physically mixed) did not show notable enhanced photocatalytic activity as compared to Bi_2O_3/WO_3 composite. This implies that there might be some interaction between Bi_2O_3 and WO_3 in Bi_2O_3/WO_3 composite sample, which played important role in improving the photocatalytic activity.

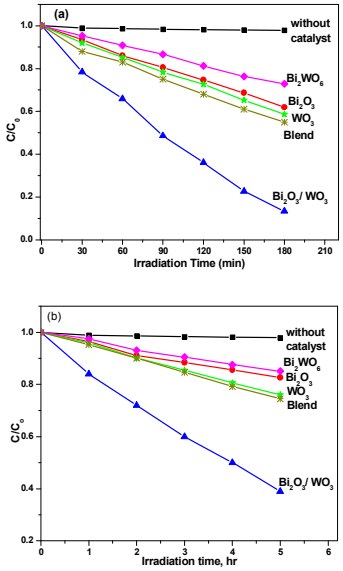

Fig. 8: Photocatalytic degradation efficiency using different catalysts activities of different catalysts under visible light irradiation; (a) RhB and (b) 4-NA

3.2.2 Kinetic and stability study

The degradations of RhB and 4-NA agree with pseudo-first order kinetics. Their photocatalytic degradation can be described by Equation 3.

$$\ln (C_o/C) = -kt \qquad (3)$$

where C_o is the initial concentration of RhB (or 4-NA), C is the concentration of RhB (or 4-NA) at time t, and k is the rate constant. The corresponding rate constants (k) were calculated and are reported in Table 2. Under the same experimental conditions, the rate constant of RhB degradation with the Bi_2O_3/WO_3 composite was determined to be 3.12 times larger than that of pristine Bi_2O_3 and 2.78 times that of WO_3. Similarly, the rate constant of 4-NA degradation with Bi_2O_3/WO_3 composite was found to be 4.32 times as large as that of pure Bi_2O_3 and 3.32 times that of WO_3. The rate constants for the composites are 4.33 and 5.24 times greater than that of Bi_2WO_6 for the degradation of RhB and 4-NA, respectively. It is also clear that the rate constants for composites are higher than those of physically mixed blend sample.

Table 2: Pseudo first order rate constants for photocatalytic degradation process of RhB or 4-NA under visible light irradiation ($\lambda \geq 420$ nm).

Sample	RhB degradation Rate constants (min^{-1})	4-NA degradation Rate constants (h^{-1})
Bi_2O_3	0.025	0.040
WO_3	0.028	0.052
Bi_2WO_6	0.018	0.033
Bi_2O_3/WO_3	0.078	0.173
blend	0.030	0.053

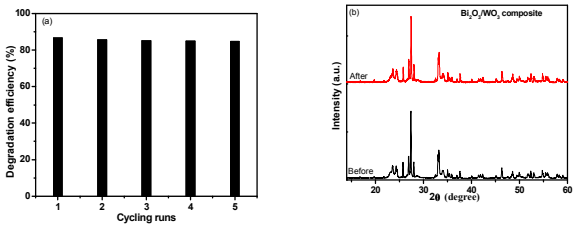

Fig. 9: Photocatalyst stability. (a) Cycling runs of Bi_2O_3/WO_3 composite under visible light irradiation for 3 hour; (b) XRD patterns of Bi_2O_3/WO_3 composite before and after photocatalytic degradation of 4-nitroaniline (4-NA).

The stability of Bi_2O_3/WO_3 composite was further investigated by recycling the photocatalyst for RhB degradation under visible light irradiation for 3 hours. During this stability test, fresh RhB solution was used after each cycle of photocatalytic experiment. The results are displayed in Fig. 9a. After five cycles, the photocatalytic ability of the Bi_2O_3/WO_3 composite was virtually unchanged (declined by only 1.87%), indicating that the Bi_2O_3/WO_3 composite photocatalyst possesses excellent photocatalytic stability and recyclability.

Furthermore, PXRD analyses of the Bi_2O_3/WO_3 composite photocatalyst before and after the reaction (4-NA degradation) shown in Fig. 9b, clearly indicate that the Bi_2O_3/WO_3 composite is photo- and chemically stable.

3.2.3 Proposed mechanism of photocatalytic activity of RhB degradation and 4-NA degradation

In the photocatalytic processes, a series of photo-induced reactive species, including h^+, $^{\bullet}OH$ or $^{\bullet}O_2^-$, directly take part in the redox process after the electron–hole pairs are generated. The electron can be trapped by molecular oxygen to produce the superoxide radical ($^{\bullet}O_2^-$), which acts as a strong oxidant to degrade dye molecules. In the photocatalytic degradation of RhB using Bi_2O_3, WO_3, Bi_2O_3/WO_3 composite, or Bi_2WO_6, the generation of hydroxyl radicals ($^{\bullet}OH$) is almost impossible because the valence band position of these catalysts lies much higher than the energy of $^{\bullet}OH/OH^-$ (1.99 eV). Hence, the photocatalytic degradation of RhB is primarily caused by superoxide radicals and photogenerated holes.[47]

In order to survey the active species in the photodegradation process of RhB over Bi_2O_3/WO_3 composite, the trapping experiments were conducted. Various scavengers, including benzoquinone (BQ), disodium salt of ethylene diamine tetra acetic acid (Na_2-EDTA) and isopropanol (IPA) were added to as the quenchers of superoxide radicals ($^{\bullet}O_2^-$), holes (h^+) and hydroxyl radicals ($^{\bullet}OH$) respectively.[41,48] From Table 1S (supporting information, ESI), it can be found that degradation efficiency of RhB was slightly affected by the addition of IPA. On the other hand, the degradation efficiency is significantly inhibited by the addition of BQ and Na_2-EDTA. These results indicated that superoxide radicals ($^{\bullet}O_2^-$) and holes (h^+) are the main active species in the degradation of RhB.[49]

Similarly, the degradation of 4-NA also follows the same pathway except that generation of the superoxide radical ($^{\bullet}O_2^-$) is unlikely because the experiment was conducted under nitrogen flow. Hence, the photogenerated holes (h^+) located in the valence band of the catalysts are solely responsible for 4-NA degradation. These holes (h^+) can produce active carbon-dioxide anion radial ($^{\bullet}CO_2^-$) in the presence of oxalate ($C_2O_4^{2-}$) ion (Equation 4). These $^{\bullet}CO_2^-$ radical anions have a strong reductive ability and hence can reduce 4-NA.[50–52]

$$C_2O_4^{2-} + h^+ \rightarrow CO_2 + {}^{\bullet}CO_2^- \qquad (4)$$

3.2.4 Enhanced activity of composite

To better understand the mechanism of the enhanced photocatalytic activity of the Bi_2O_3/WO_3 composite, the relative band positions of the two semiconductors were determined since the band-edge potential levels play a crucial role in determining the pathway of the photogenerated charge carriers in a heterojunction. The conduction band (*CB*) bottoms (E_{CB}) were calculated empirically according to Equation 5.[53–55]

$$E_{CB} = X - 0.5\,E_g + E_o \qquad (5)$$

Where E_g is the band gap energy of the semiconductor, E_o is a scale factor relating the reference electrode's redox level to the absolute vacuum scale (E_o = −4.5 eV for normal hydrogen electrode), and X is the electronegativity of the semiconductor, which can be expressed as the geometric mean of the absolute electronegativity of the constituent atoms. The X values for Bi_2O_3, WO_3, and Bi_2WO_6 were calculated to be 6.23, 6.59 and 6.36, respectively, and the band gap energies of Bi_2O_3, WO_3 and Bi_2WO_6 were determined to be 2.80 eV, 2.78 eV, and 2.95 eV, respectively (Fig. 4 and Table 1). Using equation (5) above, the conduction band bottom (E_{CB}) of, Bi_2O_3, WO_3 and Bi_2WO_6 were calculated to be 0.33 eV, 0.70 eV, and 0.38 eV, respectively. Correspondingly, the valence band tops (E_{VB}) were calculated to be 3.13 eV, 3.48 eV, and 3.33 eV. Because of the small band gaps in Bi_2O_3 and WO_3, both are excited using visible light ($\lambda \geq$ 420 nm) and corresponding photo-induced electrons and holes are generated in each component of the composite. Photogenerated electrons can be injected from the conduction band of Bi_2O_3 to the conduction band of WO_3 because of the intimate contact between the two semiconductors. Simultaneously, holes generated in the valence band of WO_3 can be transferred to that of Bi_2O_3 because of the relative band positions (Fig. 10). Thus, the photo-generated charge carriers are efficiently separated and their recombination rate is significantly reduced.[8,9,35,56,57]

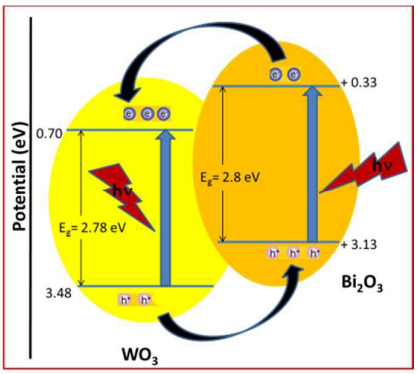

Fig. 10: Scheme for electron-hole separation and transport at the visible light driven Bi_2O_3/WO_3 composite photocatalyst with calculated band positions.

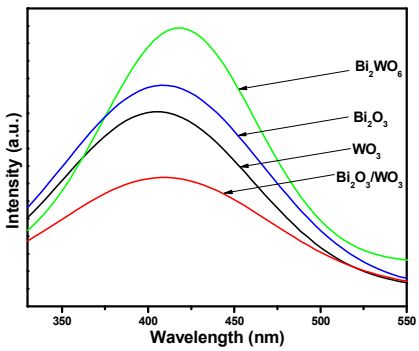

Fig. 11: Photoluminescence (PL) spectra for Bi_2O_3, WO_3, Bi_2O_3/WO_3 composite and Bi_2WO_6.

In order to investigate the lifetime of the photogenerated electron-hole pairs, photoluminescence (PL) experiments were carried out

on all prepared phases. PL spectra are related to the transfer behaviour of the photogenerated electrons and holes. In PL experiment, the electrons are excited to CB (or sub bands) from VB at certain excitation wavelength. These electrons may go back to VB giving rise to PL signal. High photoluminescence intensity is generally considered to reflect a high recombination rate of charge carriers.[41,58–60] Fig. 11 shows the PL spectra for Bi_2O_3, WO_3, Bi_2O_3/WO_3 composite and Bi_2WO_6 with an excitation wavelength of 300 nm. The main emission peak is centred at about 400-440 nm for all samples. The PL emission intensity of the composite Bi_2O_3/WO_3 is significantly smaller compared to that of the precursors Bi_2O_3, WO_3, and ternary Bi_2WO_6. The PL emission intensity was found to be in the order $Bi_2O_3/WO_3<WO_3<Bi_2O_3<Bi_2WO_6$. In addition to the PL study, we have also conducted electrochemical impedance spectra (EIS) to understand the migration and transfer process of photogenerated electron and holes. From Fig. 12, it could be seen that the diameter of the Nyquist circle of composite was significantly lower than that of the pristine Bi_2O_3 or WO_3 and ternary oxide (Bi_2WO_6). The smaller diameter of the arc implied lower resistance occurred on the surface of electrode.[31,41,48,61] This result further demonstrates that introduction of Bi_2O_3 into WO_3 can enhance the separation and transfer efficiency of photogenerated electron and holes, which is favourable for enhancing the photocatalytic activity. The results from EIS are consistent with PL. These results suggest that the composite has a much lower recombination rate of photogenerated charge carriers, consistent with the observed higher photocatalytic activity.

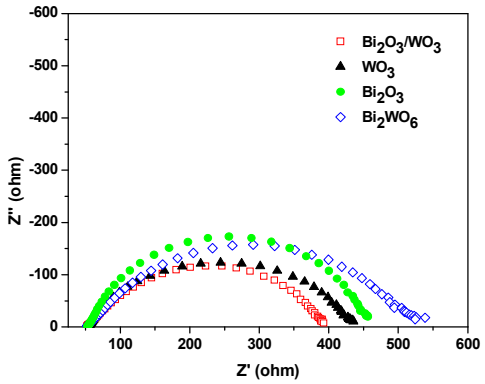

Fig. 12: Electrochemical Impedance Spectra of Bi_2O_3, WO_3, and Bi_2O_3/WO_3 composite photocatalysts.

Conclusions

In summary, Bi_2O_3/WO_3 composite photocatalyst fabricated via a hydrothermal method and its catalytic activity for RhB and 4-NA degradation was studied and compared to that of individual components and ternary oxide Bi_2WO_6. The highest degradation efficiency was achieved for the Bi_2O_3/WO_3 composite, which induced 76.67% degradation of RhB within 3 h and 60% degradation of 4-NA within 5 h under visible light irradiation, while pure WO_3 (and Bi_2O_3) led to 41.37% (38.07%) degradation of RhB and 17.03% (23.9%) degradation of 4-NA within the same time period. Similarly only 27.15% of RhB and 15% of 4-NA decomposed in the same time period when using Bi_2WO_6 under visible light irradiation. The enhanced activity is attributed to the effective separation of electron–hole pairs in the composite giving the synergetic effects between Bi_2O_3 and WO_3. Based upon the band positions, photoluminescence and electrochemical impedance data, a simple mechanism has been proposed that provides new insights for the fabrication of composite materials that have enhanced photocatalytic performance under visible light thus maximizing the use of solar energy.

Acknowledgements

A portion of this research including the STEM, UV-Vis-DRS, Raman and PL was conducted at the Center for Nanophase Materials Sciences, which is a DOE Office of Science User Facility. The authors would like to thank Dr. Corey Hewitt, Wake Forest University, Department of Physics, for his support in collecting XPS data. The authors gratefully acknowledge John Reynolds and Anna Österholm for providing access to their potentiostat for EIS measurements. Support from Phase II Triad Interuniversity Project (TIP) is acknowledged.

Notes and references

1 K. Rajeshwar, *J. Phys. Chem. Lett.*, 2011, **2**, 1301–1309.
2 A. Fujishima and K. Honda, *Nature*, 1972, **238**, 37–38.
3 F. E. Osterloh, *Chem Soc Rev*, 2013, **42**, 2294–2320.
4 R. Asahi, T. Morikawa, T. Ohwaki, K. Aoki and Y. Taga, *Science*, 2001, **293**, 269–271.
5 M. Ni, M. K. H. Leung, D. Y. C. Leung and K. Sumathy, *Renew. Sustain. Energy Rev.*, 2007, **11**, 401–425.
6 R. Abe, *J. Photochem. Photobiol. C Photochem. Rev.*, 2010, **11**, 179–209.
7 A. Zaleska, *Recent Pat. Eng.*, 2008, **2**, 157–164.
8 H. Wang, L. Zhang, Z. Chen, J. Hu, S. Li, Z. Wang, J. Liu and X. Wang, *Chem Soc Rev*, 2014, **43**, 5234–5244.
9 R. Marschall, *Adv. Funct. Mater.*, 2014, **24**, 2421–2440.
10 K. Sivula, F. L. Formal and M. Grätzel, *Chem. Mater.*, 2009, **21**, 2862–2867.
11 D. J. Ham, A. Phuruangrat, S. Thongtem and J. S. Lee, *Chem. Eng. J.*, 2010, **165**, 365 – 369.
12 K. Takehara, K. Yamazaki, M. Miyazaki, Y. Yamada, S. Ruenphet, A. Jahangir, D. Shoham, M. Okamura and M. Nakamura, *Virus Res.*, 2010, **151**, 102 – 103.
13 R. Abe, H. Takami, N. Murakami and B. Ohtani, *J. Am. Chem. Soc.*, 2008, **130**, 7780–7781.
14 M. Qamar, M. A. Gondal and Z. H. Yamani, *Catal. Commun.*, 2010, **11**, 768 – 772.
15 D. Bi and Y. Xu, *Langmuir*, 2011, **27**, 9359–9366.
16 J. Cao, B. Luo, H. Lin, B. Xu and S. Chen, *Appl. Catal. B Environ.*, 2012, **111–112**, 288–296.
17 S. A. K. Leghari, S. Sajjad, F. Chen and J. Zhang, *Chem. Eng. J.*, 2011, **166**, 906–915.
18 H. Widiyandari, A. Purwanto, R. Balgis, T. Ogi and K. Okuyama, *Chem. Eng. J.*, 2012, **180**, 323–329.
19 T. Arai, M. Yanagida, Y. Konishi, Y. Iwasaki, H. Sugihara and K. Sayama, *J. Phys. Chem. C*, 2007, **111**, 7574–7577.
20 Z. Liu, Z.-G. Zhao and M. Miyauchi, *J. Phys. Chem. C*, 2009, **113**, 17132–17137.
21 A. Hameed, V. Gombac, T. Montini, L. Felisari and P. Fornasiero, *Chem. Phys. Lett.*, 2009, **483**, 254–261.
22 M. Li, F. Li and P. G. Yin, *Chem. Phys. Lett.*, 2014, **601**, 92–97.

23 S. Y. Chai, Y. J. Kim, M. H. Jung, A. K. Chakraborty, D. Jung and W. I. Lee, *J. Catal.*, 2009, **262**, 144–149.
24 Z. Zhang, J. Zhu, S. Li and Y. Mao, *J. Solid State Chem.*, 2014, **211**, 120–123.
25 B. Naik, S. Martha and K. M. Parida, *Int. J. Hydrog. Energy*, 2011, **36**, 2794–2802.
26 X. Lin, J. Xing, W. Wang, Z. Shan, F. Xu and F. Huang, *J. Phys. Chem. C*, 2007, **111**, 18288–18293.
27 S. P. Adhikari, Z. D. Hood, K. L. More, I. Ivanov, L. Zhang, M. Gross and A. Lachgar, *RSC Adv*, 2015, **5**, 54998–55005.
28 X.-F. Cao, L. Zhang, X.-T. Chen and Z.-L. Xue, *CrystEngComm*, 2011, **13**, 306–311.
29 H. Ma, J. Shen, M. Shi, X. Lu, Z. Li, Y. Long, N. Li and M. Ye, *Appl. Catal. B Environ.*, 2012, **121–122**, 198–205.
30 G.-H. He, G.-L. He, A.-J. Li, X. Li, X.-J. Wang, Y.-P. Fang and Y.-H. Xu, *J. Mol. Catal. Chem.*, 2014, **385**, 106–111.
31 H. Huang, L. Liu, Y. Zhang and N. Tian, *RSC Adv*, 2015, **5**, 1161–1167.
32 F. Qin, G. Li, R. Wang, J. Wu, H. Sun and R. Chen, *Chem. – Eur. J.*, 2012, **18**, 16491–16497.
33 K. C. Leonard, K. M. Nam, H. C. Lee, S. H. Kang, H. S. Park and A. J. Bard, *J. Phys. Chem. C*, 2013, **117**, 15901–15910.
34 H. Fu, L. Zhang, W. Yao and Y. Zhu, *Appl. Catal. B Environ.*, 2006, **66**, 100–110.
35 Z. Zhang, W. Wang, L. Wang and S. Sun, *ACS Appl. Mater. Interfaces*, 2012, **4**, 593–597.
36 Y. Peng, Q.-G. Chen, D. Wang, H.-Y. Zhou and A.-W. Xu, *CrystEngComm*, 2015, **17**, 569–576.
37 M. Ge, Y. Li, L. Liu, Z. Zhou and W. Chen, *J. Phys. Chem. C*, 2011, **115**, 5220–5225.
38 G.-H. He, C.-J. Liang, Y.-D. Ou, D.-N. Liu, Y.-P. Fang and Y.-H. Xu, *Mater. Res. Bull.*, 2013, **48**, 2244–2249.
39 X. Li, R. Huang, Y. Hu, Y. Chen, W. Liu, R. Yuan and Z. Li, *Inorg. Chem.*, 2012, **51**, 6245–6250.
40 X.-F. Liu, Y.-K. Lai, J.-Y. Huang, S. S. Al-Deyab and K.-Q. Zhang, *J Mater Chem C*, 2015, **3**, 345–351.
41 L. Huang, H. Xu, Y. Li, H. Li, X. Cheng, J. Xia, Y. Xu and G. Cai, *Dalton Trans*, 2013, **42**, 8606–8616.
42 L. Xu, M.-L. Yin and S. (Frank) Liu, *Sci Rep*, 2014, **4**.
43 Y. Wang, Y. He, T. Li, J. Cai, M. Luo and L. Zhao, *Chem. Eng. J.*, 2012, **189–190**, 473–481.
44 J. In, I. Yoon, K. Seo, J. Park, J. Choo, Y. Lee and B. Kim, *Chem. – Eur. J.*, 2011, **17**, 1304–1309.
45 J. Low, J. Yu, Q. Li and B. Cheng, *Phys Chem Chem Phys*, 2014, **16**, 1111–1120.
46 Y. Li, J. Liu, X. Huang and J. Yu, *Dalton Trans*, 2010, **39**, 3420–3425.
47 P. Wilhelm and D. Stephan, *J. Photochem. Photobiol. Chem.*, 2007, **185**, 19–25.
48 X. Bai, L. Wang and Y. Zhu, *ACS Catal.*, 2012, **2**, 2769–2778.
49 C. Xing, Z. Wu, D. Jiang and M. Chen, *J. Colloid Interface Sci.*, 2014, **433**, 9–15.
50 W. Wu, R. Lin, L. Shen, R. Liang, R. Yuan and L. Wu, *Catal. Commun.*, 2013, **40**, 1–4.
51 K. Imamura, S. Iwasaki, T. Maeda, K. Hashimoto, B. Ohtani and H. Kominami, *Phys Chem Chem Phys*, 2011, **13**, 5114–5119.
52 W. Wu, G. Liu, S. Liang, Y. Chen, L. Shen, H. Zheng, R. Yuan, Y. Hou and L. Wu, *J. Catal.*, 2012, **290**, 13–17.
53 Z. Wei, L. Feng, J. Zhi-Ming, S. Xiao-Bo, Y. Peng-Hui, W. Xue-Ren, S. Cheng, G. Zhan-Qi and L. Liang-Sheng, *J Mater Chem A*, 2014, **2**, 13226–13231.
54 M. Long, W. Cai, J. Cai, B. Zhou, X. Chai and Y. Wu, *J. Phys. Chem. B*, 2006, **110**, 20211–20216.
55 M. A. Butler and D. S. Ginley, *J. Electrochem. Soc.*, 1978, **125**, 228–232.
56 B. Chen, Y. Deng, H. Tong and J. Ma, *Superlattices Microstruct.*, 2014, **69**, 194–203.
57 A. M. Abdulkarem, A. A. Aref, A. Abdulhabeeb, Y.-F. Li and Y. Yu, *J. Alloys Compd.*, 2013, **560**, 132–141.
58 J. Tang, Z. Zou and J. Ye, *J. Phys. Chem. B*, 2003, **107**, 14265–14269.
59 Y. Du, L. Zhao and Y. Zhang, *J. Hazard. Mater.*, 2014, **267**, 55–61.
60 M. T. Mayer, C. Du and D. Wang, *J. Am. Chem. Soc.*, 2012, **134**, 12406–12409.
61 Z. Hosseini, N. Taghavinia, N. Sharifi, M. Chavoshi and M. Rahman, *J. Phys. Chem. C*, 2008, **112**, 18686–18689.

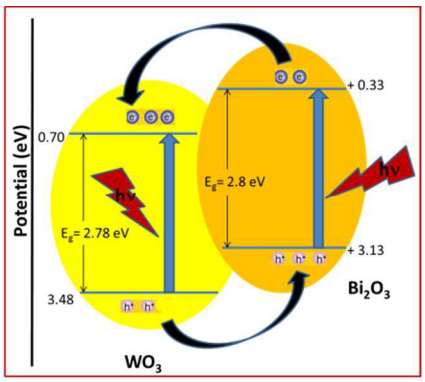

The heterojunction formed between Bi_2O_3 and WO_3 shows visible-light driven enhanced photocatalytic performance in degradation of Rhodamine b (RhB) and 4 nitroaniline (4-NA).